Estuarine, Coastal and Shelf Science 314 (2025) 109143

Contents lists available at ScienceDirect

Estuarine, Coastal and Shelf Science

journal homepage: www.elsevier.com/locate/ecss

Temporal and spatial analysis of relative sea-level changes across the Emilia-Romagna coastal plain (northern Adriatic Sea)

Matteo Meli [a,*], Marco Marcaccio [b], Marianna Mazzei [b], Claudia Romagnoli [a]

[a] Department of Biological, Geological and Environmental Sciences, University of Bologna, Bologna, Italy
[b] Agenzia Regionale Prevenzione e Ambiente (ARPAE) dell'Emilia-Romagna, Direzione Tecnica, Bologna, Italy

ARTICLE INFO

Dataset link: https://doi.org/10.5281/zenodo.14671018

Keywords:
Sea-level rise
Vertical land movement
InSAR
Satellite altimetry
Tide gauge
Emilia-Romagna coast

ABSTRACT

Sea-level rise coupled with subsidence, namely relative sea level, currently represents the greatest threat to low-lying coastal areas worldwide, leading to a constant increase in flooding risks and shoreline erosion. The Emilia-Romagna coastal plain in northern Italy, facing the Adriatic Sea, is highly urbanized and critically important to the national economy. However, the entire area is prone to high flooding risks due to its low altitude and the limited resilience of the shoreline, which also results from anthropogenic modifications mainly started from the 1950s. In this study, a refined local geocentric sea-level time series for the period 1993–2020 has been reconstructed by processing data from tide gauges and satellite altimetry. Additionally, to assess the influence of vertical land movements on the relative sea level, InSAR datasets available from 2006 to 2020 have been incorporated into the analysis. After signal processing, time series representing relative sea-level changes across the entire coastal plain were produced on a spatial grid with a resolution of 500x500 meters. A relative sea level rise, ranging from 55% to 640% stronger than the geocentric one, is observed across the entire domain, with critical spots due to localized subsidence related to underground fluid exploitation, leading to severe flooding threats.

1. Introduction

Coastal areas around the world are under threat from sea-level rise and related effects such as enhanced coastal flooding and erosion. The ongoing climate-induced sea-level rise observed at the global scale, at a rate of 3.4 ± 0.3 mm/yr over the last 30 years (IPCC, 2023), is the product of complex interactions among various factors. In detail, each coastal area experiences its own sea–level variations reflected in the relative sea level (RSL; also refer to Table 1 for all acronyms used in this work) change, i.e., the combination of geocentric sea level change (the sea surface height variation with respect to a fixed datum as the Earth's center of mass) and ongoing vertical land movements (VLMs). The latter can be caused by both natural and anthropogenic processes acting at different spatial and temporal scales (Shirzaei et al., 2021). The occurrence of subsidence, in particular, poses a significant threat to low-lying coastal areas, with potentially important environmental, social, and economic outcomes.

Recent studies on RSL (Elias et al., 2020; Anzidei et al., 2021; Palanisamy Vadivel et al., 2021) have adopted integrated observational techniques for determining VLMs, including Interferometric Synthetic Aperture Radar (InSAR) and global navigation satellite systems (GNSS), to combine these information with data on sea level. Tide gauges (TGs) provide crucial RSL observations at the local scale and, in some instances, enable century-long reconstructions. In contrast, satellite radar altimetry (SA) observes sea level in relation to a reference ellipsoid and is not affected by VLMs. While SA, which began in the early 1990 s, cannot be employed yet for long-term sea-level assessments, it facilitates the retrieval of regional-scale data and measurements far from coasts. However, a primary complication with SA sea-level measurements is that observations within approximately 15 km from the coast are contaminated by land footprint, making geophysical corrections less accurate (Cipollini et al., 2017; Vignudelli et al., 2019). To address this issue, dedicated coastal SA products have recently been developed within international projects and by space agencies (Birol et al., 2017; Cazenave et al., 2022).

The Emilia-Romagna (ER) coast, located south of the Po River Delta in northern Italy, faces the Adriatic Sea (Fig. 1a,b). This area is located on a foredeep basin experiencing natural subsidence, attributed both to tectonics and the consolidation of Quaternary alluvial deposits (Carminati and Di Donato, 1999; Amorosi et al., 2004; Teatini et al., 2011; Bruno et al., 2020). The rate of compaction of the upper

* Corresponding author.
E-mail addresses: matteo.meli7@unibo.it (M. Meli), mmarcaccio@arpae.it (M. Marcaccio), mmazzei@arpae.it (M. Mazzei), claudia.romagnoli@unibo.it (C. Romagnoli).

https://doi.org/10.1016/j.ecss.2025.109143
Received 24 July 2024; Received in revised form 5 December 2024; Accepted 15 January 2025
Available online 22 January 2025

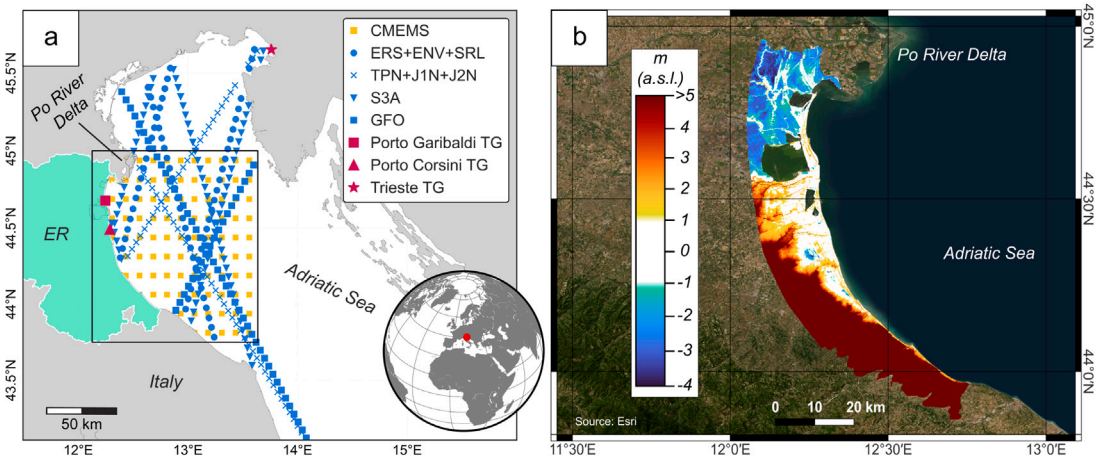

Fig. 1. (a) Location and spatial coverage of the datasets considered in this study (within the black square) for the computation of the local sea-level signal: the TGs (marked in red), the SA gridded product from CMEMS (yellow), and available missions of the X-TRACK coastal SA products in blue (refer to Section 2.2 for the acronyms). Refer to the inset globe map for the location of the area of study (red dot). (b) A detailed view of the ER coastal plain with elevation in meters above sea level (m a.s.l.). The altitude data are based on a DTM with a 5 × 5 m resolution, generated from a LiDAR acquisition in 2009 by the ER regional administration and available at https://geoportale.regione.emilia-romagna.it/download/download-data?type=raster. (For interpretation of the references to color in this figure legend, the reader is referred to the web version of this article.)

Table 1
List of the acronyms used in this work.

AR5	Assessment Report 5
ARPAE	Agenzia regionale per la prevenzione, l'ambiente e l'energia dell'Emilia-Romagna
CMEMS	Copernicus Marine Service
DTM	Digital terrain model
DUACS	Data Unification and Altimeter Combination System
ENV	Envisat
ER	Emilia-Romagna
ERS	ERS-1 and ERS-2
GIA	Glacial Isostatic Adjustment
GFO	Geosat Follow On
GNSS	Global Navigation Satellite Systems
InSAR	Interferometric Synthetic Aperture Radar
IPCC	Intergovernmental Panel on Climate Change
J1N	Jason-1 Interleaved orbit
J2N	Jason-2 Interleaved orbit
LiDAR	Light Detection and Ranging
N	Geocentric sea level
NGL14	Nevada Geodetic Laboratory
PSMSL	Permanent Service for Mean Sea Level
RSL and S	Relative sea level
SA	Satellite radar altimetry
S3A	Sentinel-3A
SONEL	Système d'Observation du Niveau des Eaux Littorales
SRL	SARAL and AltiKa
TEOS-10	Thermodynamic Equation Of Seawater
TG	Tide gauge
TPN	Topex Interleaved Orbit
VLM and U	Vertical land movement

30 m of the stratigraphic sequence has recently been estimated to be up to 1 mm/yr (Campo et al., 2017; Calabrese et al., 2024). Local subsurface facies characterized by organic-rich fine-grained sediments, associated with recent or paleoenvironments like salt marshes and swamps, are also present and even more subjected to compaction (Bruno et al., 2017). Further interactions, however, increase the complexity of the system. For instance, the occurrence of rainfall scarcity (or abundance) and related aquifer levels lead to a poro-elastic response, resulting in an increase (or decrease) in local subsidence on a seasonal time scale (Nespoli et al., 2021). Moreover, since the second half of the 20th century, a marked increase in the subsidence trend has been observed along the ER coast due to anthropogenic effects such as the withdrawal of groundwater and gas extraction (Teatini et al., 2006; Simeoni et al., 2017; Comerci and Vittori, 2019), with rates locally exceeding the natural subsidence by one order of magnitude (Bitelli et al., 2000; Carminati and Martinelli, 2002; Taramelli et al., 2015).

The ER coastal plain is a mixture of urbanized, agricultural, and natural environments, consisting of dissipative beaches with very gentle slopes, a few vegetated dunes and wetland areas around the river mouths (Perini and Calabrese, 2010). Most of the shoreline, heavily exploited for tourism, is largely protected by engineering defense structures, built to prevent erosional processes (Nordstrom et al., 2015). Since most of the ER coastal area does not exceed 2 m above mean sea level (Gambolati and Teatini, 1998), and a portion spanning up to 1200 km^2 is currently situated below it (Fig. 1b), the region is highly vulnerable to coastal flooding (Calabrese et al., 2024). Additional effects such as loss of efficiency of hydraulic structures, sea encroachment, and salt wedge intrusion significantly impact a large portion of the coastal area (Antonellini et al., 2008, 2019; Sytnik and Stecchi, 2015; Sytnik et al., 2018), further exacerbated by a negative sedimentary balance, a consequence of the reduced sediment supply from rivers (Meli and Romagnoli, 2022).

Perini et al. (2017) have developed scenarios for the combined impact of sea-level rise and subsidence on the ER coast and estimated the potential land loss using IPCC-AR5 projections to 2100 (Church et al., 2013) and subsidence rates for 2006–2011 (Bissoli et al., 2012). Since 1999, in fact, the ER Regional Agency for Prevention, Environment, and Energy (ARPAE), on behalf of the regional administration, produces and regularly updates subsidence maps for the entire region every five years, accessible at https://www.arpae.it/it/temi-ambientali/suolo/subsidenza/la-rete-regionale-di-monitoraggio-della-subsidenza. These maps generally show the average trends of vertical land movements for each sector of the region from each monitoring survey but do not represent this information over time as a time series.

In this study, to retrieve the temporal and spatial variability of RSL across the ER coastal plain, the available InSAR datasets were processed to track the evolution of VLMs in the form of time series. These information have been integrated with an updated, refined version of the local geocentric sea-level, achieved by considering data from TGs and SA. The findings have significant implications for coastal hazards and potential flooding of the coastal plain, and should be considered in future management planning and long-term adaptation policies.

2. Materials and methods

All analyses, computations, and figure production for this study were carried out using Python v.3.11 and QGIS v.3.28.12.

The relationship between VLMs (U) and geocentric sea level (N) at a specific location can be expressed by the sea-level equation (Farrell and Clark, 1976), which in its simplest form reads:

$$S = N - U \tag{1}$$

where S is RSL. Thus, to explore the evolution and spatial variability of the S parameter at the regional scale along the ER coast, signals from independent datasets have been considered and processed. In detail, to assess the N term, signals from both TGs and SA (Fig. 1a) over the period 1993–2020 were taken into account. Concurrently, the spatial and temporal variability of the U term across the ER coastal plain, over the period 2006–2020, was assessed by processing the available InSAR datasets (Fig. 2a–c) produced by TRE-ALTAMIRA, a spin-off company of the Polytechnic University of Milan, through the use of the SqueeSAR™ algorithm (Kampes, 2006; Ferretti et al., 2011). By taking into account all available data for specific areas, this algorithm identifies radar targets with stable electromagnetic responses (Perissin and Ferretti, 2007), encompassing both natural formations and anthropogenic features, and enabling millimeter-level accuracy in measuring VLMs (see https://site.tre-altamira.com/insar/ for details).

All datasets were converted to monthly averages and the seasonal cycle removed from each signal by using the Loess Decomposition method (Cleveland et al., 1990). After completing all specific processing steps, to clearly quantify the evolution and magnitude of the S term, both N and U time series were adjusted so that their monthly values for January 2006 are set to zero, establishing this month as the reference epoch. The non-parametric Theil–Sen regressor (Sen, 1968) was implemented to assess the preferred linear slope for each time series over the period of interest. As the presence of serial autocorrelation in the data leads to an underestimation of the uncertainties within trends, the corrected standard error (μ) has been computed as follows:

$$\mu = \sqrt{\frac{\sum_{i=1}^{n} res_i^2}{n-2}} \cdot \sqrt{\frac{1}{\sum_{i=1}^{n}(x_i - \overline{x})^2}} \cdot \sqrt{\frac{1+\phi_1}{1-\phi_1}} \tag{2}$$

where n is the number of valid observations, ϕ_1 is the autoregressive parameter of order 1 of the residuals, x_i represents the numerical representation of time for the ith observation, and res_i are the differences between the observed values and those predicted by the Theil–Sen regressor for the ith observation. In order to assess the statistical significance (99% confidence interval) of linear trends within the U and S time series, the non-parametric Mann–Kendall test, modified for autocorrelated data (Hamed and Ramachandra Rao, 1998), was performed. To evaluate the presence of acceleration/deceleration within the U term for the period 2006–2020 (see Section 2.4), a robust quadratic fit was applied to each time series in the dataset using ordinary least squares regression, since the Theil–Sen regressor is not suitable outside of linear analyses. To determine the significance of the quadratic term, an F-test was conducted to evaluate whether the inclusion of the quadratic term significantly improves the model fit. The p-values obtained from the F-test were used to assess the statistical significance of the quadratic trends, with a threshold of 0.01 (99% confidence interval).

2.1. Tide gauge data

The study considered three TGs (see Fig. 1a for location), Porto Garibaldi and Porto Corsini, which are located along the ER coast about 21 km far from each other, and Trieste for U correction purposes (see below). TG time series from Porto Garibaldi and Trieste were obtained from the Permanent Service for Mean Sea Level (PSMSL) (PSMSL, 2024; Holgate et al., 2013), while data from Porto Corsini were sourced from Meli and Romagnoli (2022). For the purposes of this analysis, the data from Porto Corsini and Trieste TG were restricted to the period 1993–2015, as the subsequent years for Porto Corsini exhibit significant discontinuities. Conversely, all available data from Porto Garibaldi TG, covering the period 2010–2021 at the time of this analysis, were included.

By considering monthly mean datasets, the contributions to the low-frequency local sea-level response related to the effects of atmospheric pressure were accounted for, by applying the inverse barometer (η_{IB}) correction at the TGs coordinates (x_i, y_i) and time step (t), following Dorandeu and Le Traon (1999):

$$\eta_{IB}(x_i, y_i, t) = -\frac{1}{g\rho}\left(P(x_i, y_i, t) - P_{ref}(t)\right) \tag{3}$$

where P is the mean sea-level pressure parameter from the ERA5 reanalysis dataset (Hersbach et al., 2023), and P_{ref} is its spatial mean over the global ocean and the selected period, while ρ denotes the sea water density. The latter, has been computed specifically at any TG location accounting for the Thermodynamic Equation Of Seawater (TEOS-10) (McDougall and Barker, 2011), after converting practical salinity and potential temperature values, retrieved from the Mediterranean Sea Physics Reanalysis (Escudier et al., 2021), to absolute salinity and conservative temperature, respectively. The reanalysis product (https://doi.org/10.25423/CMCC/MEDSEA_MULTIYEAR_PHY_006_004_E3R1) is freely available and currently distributed by the Copernicus Marine Service (CMEMS). Since the high-frequency response of sea level to atmospheric loading and wind becomes negligible on timescales greater than 20 days (Carrere and Lyard, 2003), the application of the η_{IB} correction removes the static effect of atmospheric pressure on the TG data. This ensures compatibility with the SA data, which are already corrected for both the inverse barometer effect and dynamic atmospheric effects through the Dynamic Atmospheric Correction. The latter includes not only the static inverse barometer effect but also the dynamic response of the ocean to wind and pressure fluctuations on shorter timescales.

The reliable removal of the U component from the TG at Porto Garibaldi has been facilitated by the presence of a co-located GNSS station. This approach ensures that the VLM signal is accurately representative of the location surrounding the TG (Santamarìa-Gòmez et al., 2012). The data were acquired from the Système d'Observation du Niveau des Eaux Littorales (SONEL) website, provided, among others, with the Nevada Geodetic Laboratory (NGL14) solution (Blewitt et al., 2016, 2018). The same procedure cannot be employed for correcting the Porto Corsini TG time series, due to the absence of a co-located GNSS station. Consequently, an alternative approach as described by Zerbini et al. (2017) and Meli and Romagnoli (2022) was adopted: initially, monthly averages from the Porto Corsini TG were subtracted from those of the Trieste TG. From the resulting residuals, a third-order polynomial regression was calculated to approximate the VLMs at Porto Corsini. This curve was then removed from the Porto Corsini time series. This method relies on the premise that VLMs at the Trieste TG site are either stable or negligible in the considered time frame, a conclusion supported by various studies (Antonioli et al., 2009; Furlani et al., 2011; Sánchez et al., 2018; Zerbini et al., 2021). Moreover, this assumption is reinforced by the fact that the dataset from the Trieste TG is considered representative of the geocentric sea level in the northern Adriatic Sea (Zerbini et al., 2021), and indeed, it is highly consistent throughout this region (Adani et al., 2011).

2.2. Altimetry data

Gridded sea surface height measurements, with a spatial resolution of 1/8° by 1/8° and fourth level of processing (L4), were retrieved from the CMEMS. This dataset (https://doi.org/10.48670/moi-00141) is produced by the Data Unification and Altimeter Combination System (DUACS) altimeter processing, incorporating data from all SA missions available at a specific time. The dataset is provided with all standard corrections already applied, including instrumental drift, sea state bias, signal refraction through the atmosphere, and the dynamic atmospheric corrections. In this work, in order to minimize the impact of TOPEX-A instrumental drift on the precision and reliability of records from 1993 to 1998, a correction was applied to the CMEMS datasets. This

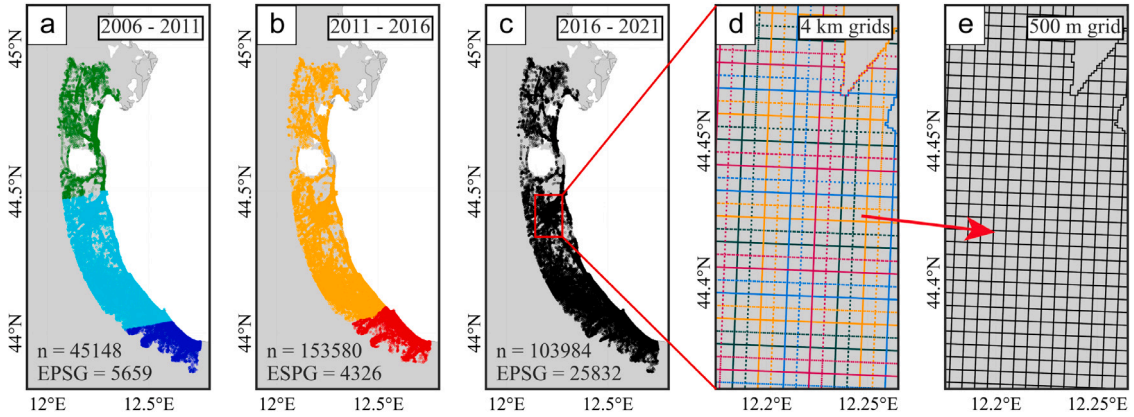

Fig. 2. (a–c) The three considered InSAR datasets, generated following various monitoring campaigns. Each scatter point corresponds to an independent time series over a specified period (noted in the upper right corner). Within the same dataset, different colors (randomly selected) signify points related to distinct acquisition time series throughout the period (i.e., observations made on different revisiting time). The EPSG information pertains to the reference system for each dataset, while n indicates the number of scatter points considered for each product. These data have already been filtered based on the coherence parameter. (d) Detail of the eight 4 × 4 km grids, each shifted by 500 m in both latitude and longitude, distinguished by color (yellow, green, blue, and red) and linestyle (solid and dotted lines). (e) The resulting final grid with a 500 × 500 m resolution obtained by averaging the 4 × 4 grids (see Section 2.4 for details).

correction (available within the same CMEMS dataset), based on global comparisons between SA and TGs, is designed for the global mean sea level but is also applicable on regional or local scales as the best estimate available (Group, 2018). All data within the region bounded by 45.00°N-43.75°N and 12.13°E-13.64°E (indicated by the black square in Fig. 1a) were considered in this work and the mean calculated. This procedure aims to derive a generalized sea-level curve representative of the area of interest, by incorporating variability from the coast to the near open sea. Considering all data located more than 10–15 km from the shoreline together with those closer, indeed, aims to reduce the loss of accuracy in the latter due to land footprint. However, it is critical to note that the implementation of state-of-the-art corrections and models within recent DUACS products has substantially improved the accuracy of measurements along the shoreline, with error reduction varying locally from 10 to 50% (Taburet et al., 2019).

To ensure the potential variability of sea level at the scale of the ER shoreline is accounted for, data from the X-TRACK SA product for coastal application were also included in the analysis. This product (version 2.1, https://doi.org/10.24400/527896/a01-2022.020) was developed and validated by CTOH/LEGOS France and currently distributed by Aviso+. SA data from X-TRACK, which consist of along-track sea level anomalies projected onto predefined reference tracks of various missions, were constructed by processing data from the following missions to encompass the entire SA period without gaps and focus solely on data proximate to the study area: ERS-1/ERS-2/Envisat / SARAL/AltiKa (ERS+ENV+SRL; covering the period from October 23, 1992, to April 16, 2016), Topex Interleaved orbit/Jason-1 Interleaved orbit / Jason-2 Interleaved orbit (TPN+J1N+J2N; from September 20, 2002, to May 13, 2017), Geosat Follow On (GFO; from January 8, 2000, to September 8, 2008), and Sentinel-3 A (S3 A; from March 12, 2016, to January 26, 2023). These are derived from the L2 Aviso+ product, with a spatial resolution of approximately 7 km between points, and are processed according to the X-TRACK strategy (Birol et al., 2017). The latter incorporates dedicated filtering and the same types of standard corrections as previously described for the CMEMS product, in this case, optimally selected to enhance the signal's response closer to the coast. These aspects, however, resulted in a noisier time series compared to products that undergo higher levels of processing, such as L3 or L4, across any point along the track. To mitigate this issue, in this work, the average was computed for spatial data over the same area defined for the CMEMS product, a method already suggested in previous studies for different contexts worldwide (Dieng et al., 2021; Oelsmann et al., 2021; Romagnoli et al., 2022).

2.3. Ensemble geocentric sea level time series

As a result of the processing described in Section 2.1, the two TGs from Porto Garibaldi and Porto Corsini were combined into a single time series, by aligning their temporal means over the shared interval of 2010–2015. The effect of Glacial Isostatic Adjustment (GIA) has been accounted for in order to remove this component from the sea-level time series. This correction was applied using the ICE-6G_C ($dRsl$ parameters for Porto Corsini and Trieste TGs and $dRad + dSea$ for both SA datasets) model from Peltier et al. (2015). Note that the GIA correction was not applied to the Porto Garibaldi TG, as the total VLMs had already been removed through the use of the co-located GNSS signal, which implicitly includes the contribution of the GIA term.

At this stage, all geocentric sea level time series showed significant correlations with one another at the 95% confidence interval, with values of 0.53 (TGs and X-TRACK), 0.56 (CMEMS and X-TRACK), and 0.65 (CMEMS and TGs), indicating robust associations between the time series within the context of the study area. These correlation coefficients were obtained using the non-parametric Kendall's Tau correlation method (Kendall, 1938), which is generally more robust and efficient than other correlation methods (Croux and Dehon, 2010), applied after linearly detrending the time series. The effect of auto-correlation on these estimates was accounted for by considering the effective sample size at lag-1 (Bartlett, 1935; Santer et al., 2000). This adjustment was implemented through a bootstrap approach, involving 100,000 iterations, to ensure robustness of the correlation results. Thus, the final ensemble local N time series (Fig. 3) was computed by taking the mean of the sea-level datasets, together with its uncertainty (1σ), following the application of datum correction (as described for TGs). The entire procedure leading to the computation of the local N was necessary to address inconsistency issues in sea-level measurements between different observational datasets, such as TG and SA, as thoroughly described in the literature (see Bruni et al. (2022) and references therein).

The ensemble time series 1σ values, as well as the combined uncertainties from both the N and U terms (see below) for the computation of the S parameter, were computed by accounting for all datasets' uncertainties using the square root of the sum of squares method:

$$1\sigma_{\text{ens}} = \sqrt{\sum_{i=1}^{n} 1\sigma_i^2} \tag{4}$$

This method ensures that the ensemble time series reflects a comprehensive estimate of uncertainty from the combined datasets.

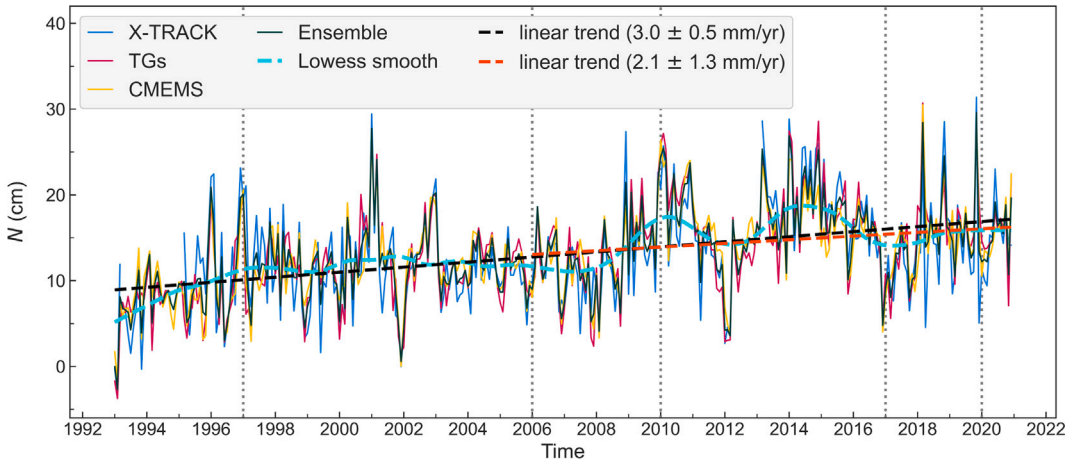

Fig. 3. The ensemble time series (dark green), along with its linear trends over different periods (1993–2020: black dashed line; 2006–2020: red dashed line) and non-linearity (Lowess smooth: cyan dashed line), represents the local geocentric sea level, incorporating all considered datasets after processing and corrections (i.e., TGs (red solid line), X-TRACK (blue solid line), CMEMS (yellow solid line)). The vertical gray dotted lines indicate the main changes in the sea-level trend, as reported in Meli et al. (2023). (For interpretation of the references to color in this figure legend, the reader is referred to the web version of this article.)

2.4. InSAR processing

Due to the low reliability and gaps in the data from the 1990 s and the first half of the 2000 s, InSAR data for assessing U were considered starting from 2006. The quantity and distribution density of InSAR data available along the ER coastal plain vary significantly over time and are heterogeneous across the datasets (Fig. 2a–c), owing to the different satellite missions available during each period. Specifically, data from Radarsat-1 (24-days revisiting time), operated by the Canadian Space Agency, were used for both the 2006–2011 and 2011–2016 surveys (Fig. 2a and b); the latter, however, also considered data from Radarsat-2 (same specifics as for Radarsat-1). On the contrary, data from Sentinel-1 constellation (12-days revisiting time) within the ESA's Copernicus Program were used for the survey 2016–2021 (Fig. 2c). As each dataset is characterized by a different spatial reference system (see Fig. 2a–c), all datasets were converted to the EPSG:4326 coordinate system for processing and the development of the final gridded product in this study.

All data were filtered to include only those with a temporal coherence index of 0.7 or higher, as recommended by Mora et al. (2003). Temporal coherence assesses how well the estimated motion follows analytical models, such as polynomial and sinusoidal ones, by comparing time series against these models to derive an index; this index ranges from 0 (unreliability) to 1 (perfect alignment). All data available within the gridded polygon (100 × 100 m) used by ARPAE for computing the subsidence maps were considered. Following these filtering steps, the portion of the ER coastal plain under analysis covers an area of almost 187,000 hectares.

A spatial refinement was implemented to achieve a gridded view of the coastal plain. This procedure entails a loss of robustness due to the reduced data available over smaller areas. To avoid significant robustness loss and generation of U signals affected by noise, a spatial averaging strategy was considered. Specifically, eight grids of 4 × 4 km, shifted 500 × 500 m each other (Fig. 2d), were used to generate an averaged signal with all datasets available within each grid square. Under these conditions, the number of data points was high enough to suppress noise and achieve a robust representation of the U evolution within each area. Finally, the height products from shifted grids were averaged by computing the mean of the mean values along with 1σ, thus achieving a refined signal within a 500 × 500 m grid (Fig. 2e).

Since each of the monitoring surveys stands alone, the achievement of temporal continuity and the progressive reconstruction of VLMs requires processing each dataset individually and ultimately concatenating the data. Indeed, all measurements are relative, both in time and space, as the analysis involves using a reference image, representing the temporal zero, to which displacement measurements are related (see Fig. 4a). To integrate different datasets within the same monitoring surveys, all data were converted from daily to monthly averages. This approach addresses the issue of differing revisiting times within surveys, as depicted in Fig. 2a–c, where some datasets are originally provided separately due to their distinct revisiting times. Given that the signal of VLMs can be generally described as a smoothed non-linear curve over time, the Loess Decomposition method was utilized not only for seasonal adjustment but also to eliminate the residual component. The monthly average of January 2006 was established as the new reference epoch (i.e., the temporal zero), from which, for every area of interest, the VLMs accumulate for each subsequent month. Since the data dispersion around the calculated mean tends to increase over time from a common starting point within each dataset (Fig. 4a), the temporal average was chosen as a representative measure of dispersion for each dataset (Fig. 4b) to avoid both overestimation and underestimation.

It is worth noting that only the data within the 2016–2021 product have been processed using double geometry, i.e., both ascending (from south to north) and descending (from north to south) lines of sight of the satellites, contrary to the previous products (2006–2011 and 2011–2016) which only considered observations achieved through an ascending trajectory (Marcaccio and Mazzei, 2023). This allowed, for the first time, the analysis of horizontal land movements, in addition to the vertical ones. However, it also revealed that using a single geometry might lead to a slight overestimation of VLMs, possibly affecting also the cumulative VLM determination for preceding periods (before 2016).

3. Results and discussion

3.1. Local geocentric sea level

The comprehensive approach employed for the reconstruction of local geocentric sea level (N term) resulted in a linear trend of 3.0 ± 0.5 mm/yr for the period 1993–2020 (Fig. 3). This scenario is fully consistent with the recent estimates by Meli et al. (2021), which reported a rate of 2.8 ± 0.5 mm/yr for the ER coast over the same time period. Although the overall evolution of the signal remains the same, slight differences arose because the updated signal was derived in this study from a broader range of datasets and a refined processing. This persistent rising trend of the sea level, in the Mediterranean context, is mostly attributed to the increase in the water mass component (Calafat et al., 2010; Pinardi et al., 2014) linked to the melting of major ice

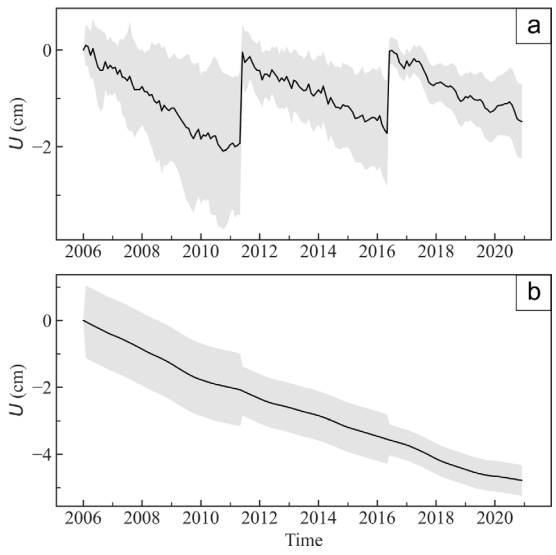

Fig. 4. (a) The time series of U means (black solid lines) from the three different datasets, by considering all data in the coastal plain, each referenced to its zero, accompanied by related 1σ (shaded gray areas). (b) The time series for the coastal plain, reconstructed after signal processing and concatenation (see Section 2.4), with all data referenced to January 2006 as the reference epoch.

sheets and continental glaciers, which is a signal transferred in the basin from the nearby Atlantic Ocean (Calafat et al., 2012). Apart from this, changes in the thermohaline properties of the water column and water mass redistribution linked to regional-to-subbasin oceanography, also known as the sterodynamic component (Gregory et al., 2019), contribute to the changes in the geocentric sea level observed during the SA period (Calafat et al., 2022), especially during the 1990 s due to a significant increase in sea surface temperature (Cazenave et al., 2001; Fenoglio-Marc, 2002).

Unlike the mass component, which contribution translates into a persistent sea-level rise, the contribution of the sterodynamic component introduces a non-linearity in the evolution of the ER geocentric sea level, as visible in Fig. 3. This prevents an accurate analysis of the presence of acceleration/deceleration in the sea-level trend over the SA period, as observed by Meli et al. (2021), as the presence of sterodynamic non-linearity produces a signal that is better represented by a piecewise linear model. Indeed, as previously observed at the scale of the Adriatic Sea (Meli et al., 2023), the local sea-level signal at the ER scale evolved with significant changes in trend occurred during specific periods. In detail, over the SA period, five inflections in the ER sea-level trend are observed (around 1997, 2006, 2010, 2017, and 2020), matching the shifts (from anticyclonic to cyclonic surficial circulation state and vice versa) of the North Ionian Gyre (Gačić et al., 2011), which fluctuates at the quasi-decadal time scale (Menna et al., 2019; Civitarese et al., 2023; Meli, 2024). This phenomenon, which originates in the Ionian Sea, triggers changes in thermohaline properties and water mass redistribution across the different sectors of the Mediterranean Sea (Malanotte-Rizzoli et al., 1997; Vilibić et al., 2020; Pirro et al., 2024), producing both momentary slowing of the rising trend and rapid jumps of sea level (Meli, 2024), the latter potentially causing a significant increase in coastal flooding and territory loss.

Further complications, among others, are induced by both inter-annual and intra-annual variability (Menna et al., 2022), which might strongly impact the sea-level signal. For instance, the magnitude of the rapid jump observed around 2010, in addition to the coincidence with one of the oceanographic shifts explained in the previous paragraph, was significantly increased by the effect of a strong negative anomaly of the North Atlantic Oscillation. This phenomenon, during the period around the winter of 2010, led to a general rise in sea level in the Mediterranean Sea by approximately 12 cm (Tsimplis et al., 2013). The effect of this phenomenon on the ER sea level is clearly visible in Fig. 3, where, according to Bonaduce et al. (2016), it should have contributed locally to a sea level rise of about 8 cm. Shortly after this event, the Adriatic sea level substantially dropped for a brief period around 2012 (Fig. 3), following a short reversal episode in the north Ionian circulation likely induced by an extreme cold winter that impacted the Adriatic area within the same year (Gačić et al., 2014).

3.2. Vertical movements of the coastal plain

Due to the limited availability of reliable InSAR data, the assessment of the U term is provided for the period 2006–2020 (Fig. 4). Downscaling information to a 500 × 500 m grid enables the spatial assessment of the U evolution over the coastal plain (Fig. 5). Only negative values (i.e., subsidence) are observed over the domain (Fig. 5a for linear trends and Fig. 5b for related uncertainties), with an average value of -3.0 ± 0.4 mm/yr and all trends statistically significant at the 99% confidence interval, even within the weakest rates (minimum subsidence value of -1.2 ± 0.3 mm/yr).

A patchy spatial distribution of the trend, with higher values (over −6 mm/yr) focusing and gradually propagating from some areas, is in accordance with previous studies (Carminati and Martinelli, 2002; Teatini et al., 2006; Taramelli et al., 2015), where it has likely been attributed to the exploitation of underground fluids. Indeed, it is well known that the most critical situation along the ER coastline is linked to gas extraction from platforms in close proximity to the shore, generating a subsidence cone that propagates to the coast (Taramelli et al., 2015) and is clearly visible on the map in Fig. 5a, centered around 44.40°N, 12.31°E. Subsidence within this area reaches a maximum rate of -14.3 ± 1.6 mm/yr over the 15 years under analysis.

Other considerable U trend values can be observed to the south of the main critical zone, extending southward to 44.1°N along the NW–SE alignment of the main urban settlements (Fig. 5a and b). Currently, no formal hypothesis has been made to link this phenomenon to a specific cause; this will be verified in terms of localized underground water depletion, intended for various uses, also as a function of reduced natural recharge of aquifers as stated by Marcaccio and Mazzei (2023). These factors may have effects on the observed spatial propagation of high U trend values, also considering that aquifers over the area are generally not horizontally confined as a consequence of a multi-layered stratigraphic architecture (Bruno et al., 2017; Campo et al., 2017).

It should be noted that most of the anthropogenically-induced subsidence rates have been reduced almost everywhere within the study area since the early 2000 s, due to the implementation of safeguard policies and the drastic reduction in underground water extraction (Preti et al., 2008; Marcaccio and Mazzei, 2023). This means that the portion of the U term not assessed in this analysis, due to the low reliability of available data (namely from 1993 to 2005), would likely yield significantly higher rates, due to the co-occurrence of much stronger subsidence phenomena (anthropogenically induced) and geocentric sea-level rise driven by various phenomena as described in Section 3.1. However, the lowering of subsidence rates is known to be the general behavior of VLMs across large portions of the ER region also over the last 15 years, as previously reported by Bissoli et al. (2012) and Marcaccio and Mazzei (2023). Indeed, if only the period 2016–2020 is considered, a maximum linear trend of −8.1 mm/yr arises within the main critical area, a value that is in agreement with reports by Marcaccio and Mazzei (2023). However, this observed value should be interpreted with caution, as a trend over just five years may be neither representative nor robust.

In order to assess how the spatial tendency of subsidence over the coastal plain is explained in terms of non-linearity, a quadratic fit analysis was employed on each reconstructed time series over the 15 years under analysis. Across the domain, about 89% of the gridded time series provide a statistically significant quadratic fit, i.e., a

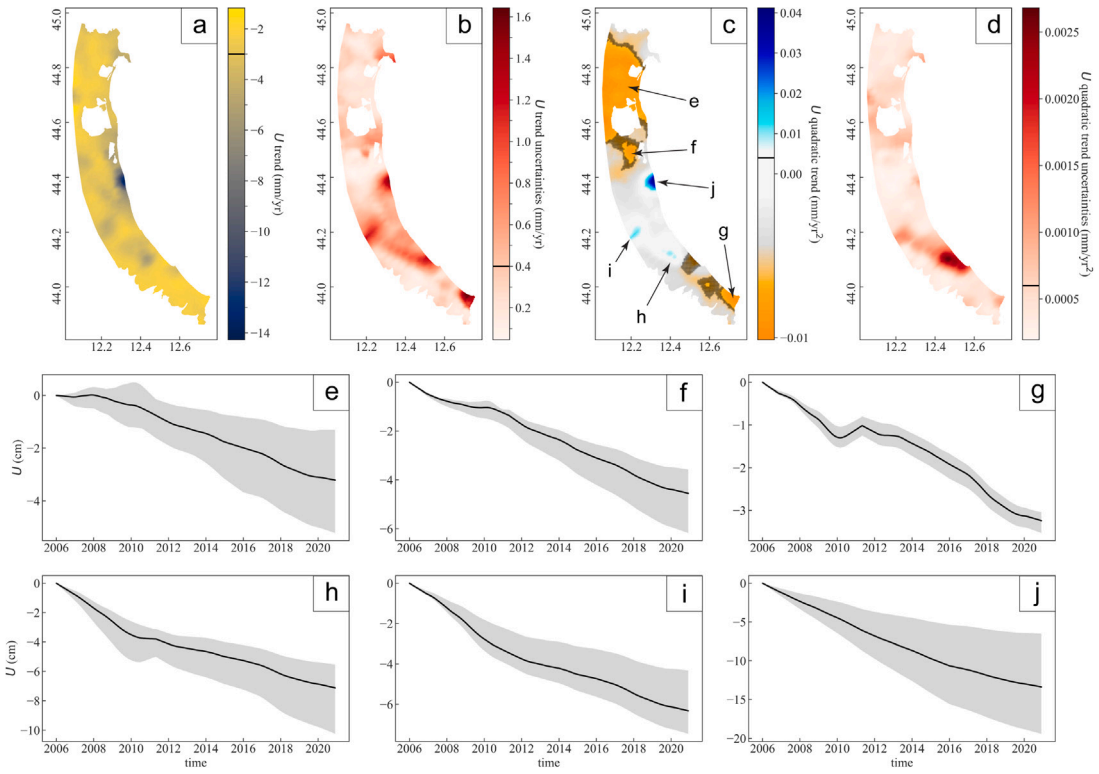

Fig. 5. (a) The spatial distribution of U linear trends for the period 2006–2020 over the entire ER coastal plain, with related uncertainties shown in (b). (c) The quadratic trends of U for the same period across the entire domain, with their uncertainties depicted in panel (d). Black dots in panel (c) indicate grid cells where the quadratic trend is not statistically significant; blueish (orange) colors represent a decreasing (increasing) tendency of the local subsidence rate; weak quadratic values, less than 0.0005 mm/yr^2 in absolute value, are shown in gray tones. Black lines within the scale bars represent the observed mean of the mapped distributions (see Section 3.2). (e–j) Time series of U (black solid lines) achieved by averaging all data which fall within each specific sector of the plain in terms of significant quadratic trends (locations indicated by black arrows in panel c); the gray shaded area represents the full range of variability observed across all the time series analyzed within each selected sector, spanning from the lowest to the highest recorded values.

significant deviation from the linear model, with an average trend of 0.004 ± 0.001 mm/yr^2 (Fig. 5c and d). A generalized slight reduction of subsidence is thus indicated by this average trend throughout the ER coastal plain; however, the spatial variability of the signal provides detailed information that might lead to local deviations from the general tendency. In this context, positive (negative) quadratic trends indicate a concave (convex) shape within the time series, which translates to a lowering (increasing) of the local subsidence rate (blueish and orange colors in Fig. 5c, respectively). However, the quadratic fit on the temporal evolution of signals might not fully represent local non-linearities. Thus, when areas with both non-significant and weak quadratic trend values (black and gray colors in Fig. 5c) are excluded, six portions of the coastal plain with specific non-linear evolution of the U term are observed (Fig. 5e–j).

In detail, over the period 2006–2020, a large part of the northern portion of the coastal plain seems to be characterized by a worsening of subsidence rate conditions, as an acceleration within the time series is generated from 2008–2010 onwards across the entire area (Fig. 5e). Indications of this ongoing process have also been reported in Marcaccio and Mazzei (2023), where trends from GNSS stations across the northern portion of the coastal plain showed slightly increasing values of VLMs over the period 2016–2021 with respect to the previous monitoring campaigns. A similar signal evolution, despite slight differences, is observed in the sector represented by Fig. 5f (refer to Fig. 5c for locations), while the acceleration detected over the southernmost portion of the coastal plain arises from a particular evolution of the signal (Fig. 5g). The latter, depicted in Fig. 5g, is mostly generated by a brief, abrupt inversion of U tendency from 2010 to 2012, followed by the reestablishment of the tendency that was present before these three years.

Conversely, a gradual reduction of subsidence rates is observed within all the critical areas described above (blueish colors in Fig. 5c), reaching a maximum quadratic trend value of 0.041 ± 0.001 mm/yr^2. This, as mentioned before, is likely primarily related to the reduction or regulation of underground fluid extraction activities (Marcaccio and Mazzei, 2023), which began in the 1990 s/2000 s and continued thereafter. However, despite the similar contributing cause generating deceleration in the time series, the three observed sectors depicted in Fig. 5h–j show different evolution over time, suggesting different processes that might have triggered the local lowering of subsidence.

Overall, it is worth noting that the stronger negative quadratic trend value observed (−0.010 ± 0.001 mm/yr^2) is roughly four times lower than the stronger positive quadratic trend value (Fig. 5c). Therefore, the observed increase of local subsidence should be interpreted with caution, as it could simply be due to the short length of the series and might be completely nullified with the inclusion of additional years of observations. It cannot be excluded that, in the northern sector of the coastal plain, factors like aquifer recharge or sediment compaction of buried paleo-peatlands might trigger worsening subsidence conditions by lowering the above soils (Bruno et al., 2020, 2024). Thus, the causes behind this, as well as the brief abrupt VLM change observed in the southernmost portion of the coastal plain or the different drivers acting in areas with subsidence lowering, need to be explored further.

3.3. Relative sea-level term

During the period 2006–2020, the N trend is 2.1 ± 1.3 mm/yr (Fig. 3), which is slower than the full-length series, primarily due to the removal of the contribution from the strong sea-level rise that occurred in the 1990 s (as described in Section 3.1). Additionally, the associated uncertainty is greater due to the reduced robustness linked to

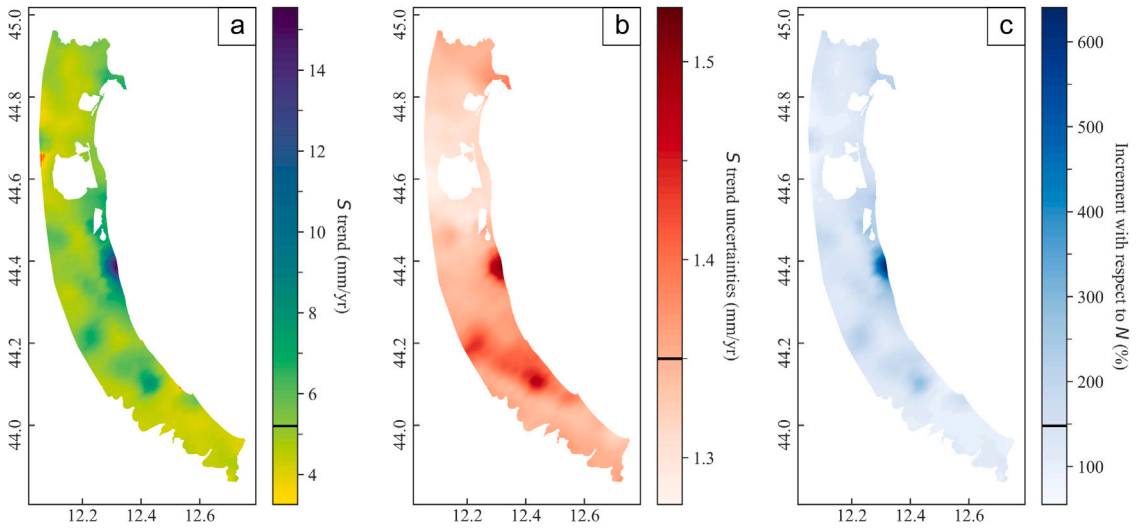

Fig. 6. (a) The mapped distribution of S trends from 2006 to 2020 across the ER coastal plain. Red points indicate a lack of statistical significance in the trend. (b) The magnitude of uncertainty in the S trend at any grid point on the map. (c) The percentage increase in S trends compared to the N trend over the same period. Black lines within the scale bars represent the average values of the mapped distributions (see Section 3.3).

the shorter time span available for computing the trend. The evaluation of the coupled interaction between N and U over the same period revealed a generalized rising S trend throughout the coastal plain, with only about 0.2% of the time series indicating a non-statistically significant trend (mostly due to the shortness of the series), that is more than twice that observed for N. In detail, the analysis revealed a mean S trend of 5.20 ± 1.35 mm/yr (Fig. 6a and b), indicating an increase of approximately 148% (Fig. 6c) compared to the local geocentric estimation, underscoring the critical contribution of VLMs in the ER coastal plain.

The analysis yields a maximum rising value of S at 15.55 ± 1.31 mm/yr in correspondence of the most critical area (see Section 3.2), which translates into an increase of 640% compared to N over just 15 years (see Fig. 6c for the percentage increase spatial distribution). On the other hand, the minimum value obtained from this analysis for the period 2006–2020 indicates an S trend of 3.26 ± 1.30 mm/yr, which represents an increase of approximately 55% compared to the local N. These percentages might have been significantly higher if the U term had been available since the early 1990 s and if there had not been a drastic reduction in subsidence induced by the safeguard policies on fluid extraction (see Section 3.2). Furthermore, the observed acceleration/deceleration in the U term might be exacerbated or mitigated by the non-linearity of N, previously discussed in Section 3.1.

Although information on S are commonly derived from TGs, i.e., a single point along the coast, the 500 × 500 m grid reconstruction can be interpreted as the elevation change over the period in a specific area of the coastal plain relative to the local sea level. Essentially, it represents a change in the base-level (Wheeler, 1964) for each cell, extending kilometers inland from the coastline. Since N is here considered consistent at the ER coastal scale, as previously observed by Meli et al. (2021), the variability detected from 2006 to 2020 in the S parameter is attributed to the influence of VLMs, as delineated in the trends map shown in Fig. 6a (see Fig. 6b for related uncertainty in spatial trend distribution), which follows the same pattern observed in Fig. 5a.

In practical terms, the reconstruction of the relative sea-level in the ER coastal plain (map of Fig. 6a) could be seen as a gridded distribution of virtual TG records across the entire domain, extending up to approximately 17 km inland and not just located along the shoreline. Despite being desirable, it is impractical to have a large number of TGs along a coastal strip, primarily due to maintenance costs and the time needed for time series to become long enough to allow accurate analysis. Indeed, while a TG provides very robust local information, it cannot be considered representative of an entire domain, primarily due to the spatial variability of VLMs. In this context, the reconstruction of the S parameter for each point on the grid allows for an assessment of the potential evolution of the combined effect of the local terms N and U.

This approach provides a novel perspective in the ER context, as it shows that not only the coastline but also the entire coastal plain is affected by the evolution of S. Therefore, the reconstruction of S at the areal scale, by integrating different datasets, may be crucial not only for assessing flooding risks across various regions and the hazards related to urbanization and public goods within the coastal plain, but also, for example, in understanding how this process might influence the river drainage and related hydrogeological management (Giambastiani et al., 2020; Soboyejo et al., 2021).

4. Conclusions

The determination of sea-level variation at the local scale is crucial for coastal hazard assessment and for adaptation strategies, considering that the impacts of sea-level rise at some coastal areas can be significantly higher than those expected from global estimates. The assessment of potential sea-level rise at the regional to local scale represents, in fact, a major source of uncertainty for mid- and long-term coastal management and adaptation policies (Bisaro et al., 2024).

In this study, a relative sea-level change time series in the ER coastal plain for 2006–2020 is reconstructed on a spatial grid of 500 × 500 m, by integrating data on the geocentric sea-level and on VLMs, acquired with high-resolution observational techniques (TG–SA and InSAR, respectively). On average, the ER coastal plain has experienced a relative sea-level rise of 5.20 ± 1.35 mm/yr over the considered period, which represents an increase of approximately 148% compared to the geocentric sea-level rise during the same period (2.1 ± 1.3 mm/yr), due to the influence of subsidence. However, the latter is characterized by significant spatial variability, which, in some areas, has caused this increase to reach a maximum of approximately 640% over just 15 years. This comprehensive approach represents a promising tool, both in terms of precision and cost-effective implementation, to better define local relative sea-level trends and to anticipate the impacts of future sea level rise in this low-lying area. The study not only focuses on the narrow ER coastal stretch but also extends its analysis to the whole coastal plain, where many areas are presently below the mean sea level and potentially impacted by sea-level rise and its associated effects.

The reconstructed temporal and spatial variability of relative sea level across the coastal plain highlights the occurrence of the most critical areas, with trend values reaching almost 16 mm/yr within the considered time frame. These areas exhibit higher subsidence rates due to both local anthropogenically-induced effects and the impact of climate change on underground aquifer recharge, although these rates appear to be under reduction. On the other side, natural fluctuations in sea level may occur periodically with non-linear behavior, amplifying or reducing this signal.

Despite the main limitation linked to the short temporal availability of high-quality InSAR data, a gridded view of the relative sea-level parameter at the coastal plain scale allows for a comprehensive understanding of the base-level change phenomenon. By considering the new information provided here, future studies will be able to shed light on the dynamic response of the shoreline and coastal plain to changes induced by multiple natural and anthropogenic factors. Additionally, this approach will likely help projecting local flooding hazard scenarios into the near future, based on parameters that go beyond the simple and common static "bathtub" approach.

CRediT authorship contribution statement

Matteo Meli: Writing – original draft, Visualization, Validation, Software, Methodology, Investigation, Formal analysis, Data curation, Conceptualization. **Marco Marcaccio:** Writing – review & editing, Resources, Methodology. **Marianna Mazzei:** Writing – review & editing, Resources. **Claudia Romagnoli:** Writing – review & editing, Writing – original draft, Supervision.

Declaration of competing interest

The authors declare that they have no known competing financial interests or personal relationships that could have appeared to influence the work reported in this paper.

Acknowledgments

This study was carried out within the RETURN Extended Partnership and received funding from the European Union Next–GenerationEU (National Recovery and Resilience Plan – NRRP, Mission 4, Component 2, Investment 1.3 – D.D. 1243 2/8/2022, PE0000005).

Funding

This work did not receive external funding.

Data availability

The main outcome products from this study are freely available at https://doi.org/10.5281/zenodo.14671018.

References

Adani, M., Dobricic, S., Pinardi, N., 2011. Quality assessment of a 1985–2007 mediterranean sea reanalysis. J. Atmos. Ocean. Technol. 28 (4), 569–589. http://dx.doi.org/10.1175/2010JTECHO798.1.

Amorosi, A., Colalongo, M.L., Fiorini, F., Fusco, F., Pasini, G., Vaiani, S.C., Sarti, G., 2004. Palaeogeographic and palaeoclimatic evolution of the Po Plain from 150–ky core records. Glob. Planet. Change 40 (1), 55–78. http://dx.doi.org/10.1016/S0921-8181(03)00098-5.

Antonellini, M., Giambastiani, B.M.S., Greggio, N., Bonzi, L., Calabrese, L., Luciani, P., Perini, L., Severi, P., 2019. Processes governing natural land subsidence in the shallow coastal aquifer of the Ravenna coast, Italy. CATENA 172, 76–86. http://dx.doi.org/10.1016/j.catena.2018.08.019.

Antonellini, M., Mollema, P., Giambastiani, B.M.S., Bishop, K., Caruso, L., Minchio, A., Pellegrini, L., Sabia, M., Ulazzi, E., Gabbianelli, G., 2008. Salt water intrusion in the coastal aquifer of the southern Po Plain, Italy. Hydrogeol. J. 16, 1541–1556. http://dx.doi.org/10.1007/s10040-008-0319-9.

Antonioli, F., Ferranti, L., Fontana, A., Amorosi, A., Bondesan, A., Braitenberg, C., Dutton, A., Fontolan, G., Furlani, S., Lambeck, K., Mastronuzzi, G., Monaco, C., Spada, G., Stocchi, P., 2009. Holocene relative sea–level changes and vertical movements along the Italian and Istrian coastlines. Quat. Int. 206 (1), 102–133. http://dx.doi.org/10.1016/j.quaint.2008.11.008.

Anzidei, M., Scicchitano, G., Scardino, G., Bignami, C., Tolomei, C., Vecchio, A., Serpelloni, E., De Santis, V., Monaco, C., Milella, M., Piscitelli, A., Mastronuzzi, G., 2021. Relative sea–level rise scenario for 2100 along the Coast of South Eastern Sicily (Italy) by InSAR data, satellite images and high–resolution topography. Remote Sens. 13 (6), http://dx.doi.org/10.3390/rs13061108.

Bartlett, M.S., 1935. Some aspects of the time–correlation problem in regard to tests of significance. J. R. Stat. Soc. 98 (3), 536–543, doi:http://www.jstor.org/stable/2342284.

Birol, F., Fuller, N., Lyard, F., Cancet, M., Niño, F., Delebecque, C., Fleury, S., Toublanc, F., Melet, A., Saraceno, M., Léger, F., 2017. Coastal applications from nadir altimetry: Example of the X–TRACK regional products. Adv. Space Res. 59 (4), 936–953. http://dx.doi.org/10.1016/j.asr.2016.11.005.

Bisaro, A., Galluccio, G., Fiorini Beckhauser, E., Romagnoli, C., McEvoy, S., Sini, E., Biddau, F., David, R., d'Hont, F., Le Cozannet, G., Pérez Gómez, B., Góngora Zurro, A., Slinger, J., 2024. Sea level rise in Europe: Governance context and challenges. State Planet Discuss. 2024, 1–52. http://dx.doi.org/10.5194/sp-2023-37, URL https://sp.copernicus.org/preprints/sp-2023-37/.

Bissoli, R., Pellegrino, I., Rapino, A., 2012. Rilievo della subsidenza nella pianura emiliano–romagnola. Relazione finale, seconda fase. Technical Report. Regione Emilia–Romagna, Arpa Emilia–Romagna, Bologna, Italy. https://www.arpae.it/it/temi-ambientali/suolo/rapporti/rapporti-subsidenza/rilievo-della-subsidenza-nella-pianura-er-seconda-fase-2012.pdf/view. (Accessed 28 June 2024).

Bitelli, G., Bonsignore, F., Unguendoli, M., 2000. Levelling and GPS networks to monitor ground subsidence in the Southern Po Valley. J. Geodyn. 30 (3), 355–369. http://dx.doi.org/10.1016/S0264-3707(99)00071-X.

Blewitt, G., Hammond, W.C., Kreemer, C., 2018. Harnessing the GPS data explosion for interdisciplinary science. Eos http://dx.doi.org/10.1029/2018EO104623.

Blewitt, G., Kreemer, C., Hammond, W.C., Gazeaux, J., 2016. MIDAS robust trend estimator for accurate GPS station velocities without step detection. J. Geophys. Res.: Solid Earth 121 (3), 2054–2068. http://dx.doi.org/10.1002/2015JB012552.

Bonaduce, A., Pinardi, N., Oddo, P., Spada, G., Larnicol, G., 2016. Sea–level variability in the Mediterranean Sea from altimetry and tide gauges. Clim. Dyn. 47, 2851–2866. http://dx.doi.org/10.1007/s00382-016-3001-2.

Bruni, S., Fenoglio, L., Raicich, F., Zerbini, S., 2022. On the consistency of coastal sea–level measurements in the Mediterranean Sea from tide gauges and satellite radar altimetry. J. Geod. 96, http://dx.doi.org/10.1007/s00190-022-01626-9.

Bruno, L., Amorosi, A., Severi, P., Costagli, B., 2017. Late Quaternary aggradation rates and stratigraphic architecture of the southern Po Plain, Italy. Basin Res. 29 (2), 234–248. http://dx.doi.org/10.1111/bre.12174.

Bruno, L., Campo, B., Costagli, B., Stouthamer, E., Teatini, P., Zoccarato, C., Amorosi, A., 2020. Factors controlling natural subsidence in the Po Plain. Proc. Int. Assoc. Hydrol. Sci. 382, 285–290. http://dx.doi.org/10.5194/piahs-382-285-2020.

Bruno, L., Meli, M., Garberi, M.L., 2024. Human–induced landscape modification in the in the last two centuries in the Po delta plain (Northern Italy). Anthropocene 48, 100453. http://dx.doi.org/10.1016/j.ancene.2024.100453.

Calabrese, L., Correggiari, A., Perini, L., Remia, A., 2024. La Geologia tra la Terra e il Mare. Strumenti per la gestione dei rischi costieri in Emilia–Romagna. Centro Stampa Regione Emilia–Romagna, http://dx.doi.org/10.5281/zenodo.10810185.

Calafat, F.M., Chambers, D.P., Tsimplis, M.N., 2012. Mechanism of decadal sea level variability in the eastern North Atlantic and the Mediterranean Sea. J. Geophys. Res. 117, C09022. http://dx.doi.org/10.1029/2012JC008285.

Calafat, F., Frederikse, T., Horsburgh, K., 2022. The sources of sea–level changes in the Mediterranean Sea since 1960. J. Geophys. Res.: Oceans 127, e2022JC019061. http://dx.doi.org/10.1029/2022JC019061.

Calafat, F.M., Marcos, M., Gomis, D., 2010. Mass contribution to the Mediterranean Sea level variability for the period 1948–2000. Glob. Planet. Change 73, 193–201. http://dx.doi.org/10.1016/j.gloplacha.2010.06.002.

Campo, B., Amorosi, A., Vaiani, S.C., 2017. Sequence stratigraphy and late Quaternary paleoenvironmental evolution of the Northern Adriatic coastal plain (Italy). Palaeogeogr. Palaeoclimatol. Palaeoecol. 466, 265–278. http://dx.doi.org/10.1016/j.palaeo.2016.11.016.

Carminati, E., Di Donato, G., 1999. Separating natural and anthropogenic vertical movements in fast subsiding areas: The Po Plain (N. Italy) Case. Geophys. Res. Lett. 26 (15), 2291–2294. http://dx.doi.org/10.1029/1999GL900518.

Carminati, E., Martinelli, G., 2002. Subsidence rates in the Po Plain, northern Italy: the relative impact of natural and anthropogenic causation. Eng. Geol. 66 (3), 241–255. http://dx.doi.org/10.1016/S0013-7952(02)00031-5.

Carrere, L., Lyard, F., 2003. Modeling the barotropic response of the global ocean to atmospheric wind and pressure forcing – comparison with observations. Geophys. Res. Lett. 30 (6), 1275. http://dx.doi.org/10.1029/2002GL016473.

Cazenave, A., Cabanes, C., Dominh, K., Mangiarotti, S., 2001. Recent sea level change in the Mediterranean Sea revealed by Topex/Poseidon satellite altimetry. Geophys. Res. Lett. 28, 1607–1610. http://dx.doi.org/10.1029/2000GL012628.

Cazenave, A., Gouzenes, Y., Birol, F., Passaro, M., Calafat, F.M., Shaw, A., Nino, F., Legeais, J.F., Oelsmann, J., Restano, M., Benveniste, J., 2022. Sea level along the world's coastlines can be measured by a network of virtual altimetry stations. Commun. Earth Env. 3, http://dx.doi.org/10.1038/s43247-022-00448-z.

Church, J.A., Clark, P.U., Cazenave, A., Gregory, J.M., Jevrejeva, S., Levermann, A., Merrifield, M.A., Milne, G.A., Nerem, R.S., Nunn, P.D., Payne, A., Pfeffer, W., Stammer, D., Unnikrishnan, A., 2013. Sea level change. In: Climate Change 2013: The Physical Science Basis. Contribution of Working Group I To the Fifth Assessment Report of the Intergovernmental Panel on Climate Change. Cambridge University Press, Cambridge, UK, pp. 1138–1191.

Cipollini, P., Calafat, F.M., Jevrejeva, J., Melet, A., Prandi, P., 2017. Monitoring sea level in the coastal zone with satellite altimetry and tide gauges. Surv. Geophys. 38, 33–57. http://dx.doi.org/10.1007/s10712-016-9392-0.

Civitarese, G., Gačić, M., Batistić, M., Bensi, M., Cardin, V., Dulčić, J., Garić, R., Menna, M., 2023. The BiOS mechanism: History, theory, implications. Prog. Oceanogr. 216, 103056. http://dx.doi.org/10.1016/j.pocean.2023.103056.

Cleveland, R.B., Cleveland, W.S., McRae, J.E., Terpening, I., 1990. STL: A seasonal–trend decomposition procedure based on loess. J. Off. Stat. 6, 3–33.

Comerci, V., Vittori, E., 2019. The need for a standardized methodology for quantitative assessment of natural and anthropogenic land subsidence: The agosta (Italy) gas field case. Remote Sens. 11 (10), http://dx.doi.org/10.3390/rs11101178.

Croux, C., Dehon, C., 2010. Influence functions of the Spearman and Kendall correlation measures. Stat. Methods Appl. 19, 497–515. http://dx.doi.org/10.1007/s10260-010-0142-z.

Dieng, H.B., Cazenave, A., Gouzenes, Y., Sow, B.A., 2021. Trends and inter–annual variability of altimetry–based coastal sea level in the Mediterranean Sea: Comparison with tide gauges and models. Adv. Space Res. 68 (8), 3279–3290. http://dx.doi.org/10.1016/j.asr.2021.06.022.

Dorandeu, J., Le Traon, P.Y., 1999. Effects of global mean atmospheric pressure variations on mean sea level changes from TOPEX/poseidon. J. Atmos. Ocean. Tech. 16, 1279–1283. http://dx.doi.org/10.1175/1520-0426(1999)016<1279:EOGMAP>2.0.CO;2.

Elias, P., Benekos, G., Perrou, T., Parcharidis, I., 2020. Spatio–temporal assessment of land deformation as a factor contributing to relative sea level rise in coastal urban and natural protected areas using multi–source earth observation data. Remote Sens. 12 (14), http://dx.doi.org/10.3390/rs12142296.

Escudier, R., Clementi, E., Cipollone, A., Pistoia, J., Drudi, M., Grandi, A., Lyubartsev, V., Lecci, R., Aydogdu, A., Delrosso, D., Omar, M., Masina, S., Coppini, G., Pinardi, N., 2021. A high resolution reanalysis for the mediterranean sea. Front. Earth Sci. 9, doi:https://www.frontiersin.org/articles/10.3389/feart.2021.702285.

Farrell, W.E., Clark, J.A., 1976. On postglacial sea level. Geophys. J. Int. 46 (3), 647–667. http://dx.doi.org/10.1111/j.1365-246X.1976.tb01252.x.

Fenoglio-Marc, L., 2002. Long–term sea level change in the Mediterranean Sea from multi–satellite altimetry and tide gauges. Phys. Chem. Earth 27, 1419–1431. http://dx.doi.org/10.1016/S1474-7065(02)00084-0.

Ferretti, A., Fumagalli, A., Novali, F., Prati, C., Rocca, F., Rucci, A., 2011. A new algorithm for processing interferometric data–stacks: SqueeSAR. IEEE Trans. Geosci. Remote Sens. 49 (9), 3460–3470. http://dx.doi.org/10.1109/TGRS.2011.2124465.

Furlani, S., Biolchi, S., Cucchi, F., Antonioli, F., Busetti, M., Melis, R., 2011. Tectonic effects on Late Holocene sea level changes in the Gulf of Trieste (NE Adriatic Sea, Italy). Quat. Int. 232 (1), 144–157. http://dx.doi.org/10.1016/j.quaint.2010.06.012.

Gačić, M., Civitarese, G., Eusebi Borzelli, G.L., Kovačević, V., Poulain, P.-M., Theocharis, A., Menna, M., Catucci, A., Zarokanellos, N., 2011. On the relationship between the decadal oscillations of the northern Ionian Sea and the salinity distributions in the eastern Mediterranean. J. Geophys. Res.: Oceans 116 (C12), http://dx.doi.org/10.1029/2011JC007280.

Gačić, M., Civitarese, G., Kovačević, V., Ursella, L., Bensi, M., Menna, M., Cardin, V., Poulain, P.-M., Cosoli, S., Notarstefano, G., Pizzi, C., 2014. Extreme winter 2012 in the Adriatic: an example of climatic effect on the BiOS rhythm. Ocean Sci. 10 (3), 513–522. http://dx.doi.org/10.5194/os-10-513-2014.

Gambolati, G., Teatini, P., 1998. Numerical analysis of land subsidence due to natural compaction of the upper Adriatic Sea Basin. In: CENAS: Coastline Evolution of the Upper Adriatic Sea Due To Sea Level Rise and Natural and Anthropogenic Land Subsidence, Edited By: Gambolati, G.. Springer Netherlands, Dordrecht, The Netherlands, pp. 103–131. http://dx.doi.org/10.1007/978-94-011-5147-4_5.

Giambastiani, B.M.S., Macciocca, V.R., Molducci, M., Antonellini, M., 2020. Factors affecting water drainage long–time series in the salinized low–Lying Coastal Area of Ravenna (Italy). Water 12 (1), http://dx.doi.org/10.3390/w12010256.

Gregory, J.M., Griffies, S.M., Hughes, C.W., Lowe, J.A., Church, J.A., Fukimori, I., Gomez, N., Kopp, R., Landered, F., Cozannet, G.L., Ponte, R.M., Stammer, D., Tamisiea, M.E., van de Wal, R.S.W., 2019. Concepts and terminology for sea level: Mean, variability and change, both local and global. Surv. Geophys. 40, 1251–1289. http://dx.doi.org/10.1007/s10712-019-09525-z.

Group, W.G.S.L.B., 2018. Global sea–level budget 1993–present. Earth Syst. Sci. Data 10 (3), 1551–1590. http://dx.doi.org/10.5194/essd-10-1551-2018, URL https://essd.copernicus.org/articles/10/1551/2018/.

Hamed, K.H., Ramachandra Rao, A., 1998. A modified Mann–Kendall trend test for autocorrelated data. J. Hydrol. 204 (1), 182–196. http://dx.doi.org/10.1016/S0022-1694(97)00125-X.

Hersbach, H., et al., 2023. ERA5 hourly data on single levels from 1940 to present. http://dx.doi.org/10.24381/cds.adbb2d47, (Accessed 02 September 2023).

Holgate, S.J., Matthews, A., Woodworth, P.L., Rickards, L.J., Tamisiea, M.E., Bradshaw, E., Foden, P.R., Gordon, K.M., Jevrejeva, S., Pugh, J., 2013. New data systems and products at the permanent service for mean sea level. J. Coast. Res. 29 (3), 493–504. http://dx.doi.org/10.2112/JCOASTRES-D-12-00175.1.

IPCC, 2023. Ocean, cryosphere and sea level change. In: Climate Change 2021 – the Physical Science Basis: Working Group I Contribution To the Sixth Assessment Report of the Intergovernmental Panel on Climate Change. Cambridge University Press, pp. 1211–1362. http://dx.doi.org/10.1017/9781009157896.011.

Kampes, B., 2006. Radar Interferometry: Persistent Scatterer Technique. Springer–Verlag, Dordrecht, The Netherlands.

Kendall, M.G., 1938. A new measure of rank correlation. Biometrika 30 (1–2), 81–93. http://dx.doi.org/10.1093/biomet/30.1-2.81.

Malanotte-Rizzoli, P., Manca, B.B., D'Alcalà, M.R., Theocharis, A., Bergamasco, A., Bregant, D., Budillon, G., Civitarese, G., Georgopoulos, D., Michelato, A., Sansone, E., Scarazzato, P., Souvermezoglou, E., 1997. A synthesis of the Ionian Sea hydrography, circulation and water mass pathways during POEM-Phase I. Prog. Oceanogr. 39 (3), 153–204. http://dx.doi.org/10.1016/S0079-6611(97)00013-X.

Marcaccio, M., Mazzei, M., 2023. Monitoraggio dei movimenti verticali del suolo e aggiornamento della cartografia di subsidenza nella pianura dell'Emilia–Romagna. Periodo 2016–2021. Technical Report. Regione Emilia–Romagna, Arpae Emilia–Romagna, Bologna, Italy. https://www.arpae.it/it/temi-ambientali/suolo/rapporti/rapporti-subsidenza/monitoraggio-movimenti-verticali-suolo-e-cartografia-subsidenza-emilia-romagna-2016-2021.zip/view. (Accessed 28 June 2024).

McDougall, T.J., Barker, P.M., 2011. Getting started with TEOS–10 and the Gibbs Seawater (GSW) Oceanographic Toolbox. SCOR/IAPSO.

Meli, M., 2024. The potential recording of North Ionian Gyre's reversals as a decadal signal in sea level during the instrumental period. Sci. Rep. 14, 4907. http://dx.doi.org/10.1038/s41598-024-55579-4.

Meli, M., Camargo, C.M.L., Olivieri, M., Slangen, A.B.A., Romagnoli, C., 2023. Sea–level trend variability in the Mediterranean during the 1993–2019 period. Front. Mar. Sci. 10, 1150488. http://dx.doi.org/10.3389/fmars.2023.1150488.

Meli, M., Olivieri, M., Romagnoli, C., 2021. Sea–level change along the emilia–Romagna Coast from tide gauge and satellite altimetry. Remote Sens. 13, 97. http://dx.doi.org/10.3390/rs13010097.

Meli, M., Romagnoli, C., 2022. Evidence and implications of hydrological and climatic change in the Reno and Lamone River Basins and Related Coastal Areas (Emilia–Romagna, Northern Italy) over the last century. Water 14, 2650. http://dx.doi.org/10.3390/w14172650.

Menna, M., Gačić, M., Martellucci, R., Notarstefano, G., Fedele, G., Mauri, E., Gerin, R., Poulain, P.-M., 2022. Climatic, decadal, and interannual variability in the upper layer of the mediterranean sea using remotely sensed and in–situ data. Remote Sens. 14 (6), http://dx.doi.org/10.3390/rs14061322.

Menna, M., Reyes-Suarez, N.C., Civitarese, G., Gačić, M., Poulain, P.-M., Rubino, A., 2019. Decadal variations of circulation in the central mediterranean and its interactions with the mesoscale gyres. Deep- Sea Res.: II Top. Stud. Ocean. 164, 14–24. http://dx.doi.org/10.1016/j.dsr2.2019.02.004.

Mora, O., Mallorqui, J.J., Broquetas, A., 2003. Linear and nonlinear terrain deformation maps from a reduced set of interferometric SAR images. IEEE Trans. Geosci. Remote Sens. 41 (10), 2243–2253. http://dx.doi.org/10.1109/TGRS.2003.814657.

Nespoli, M., Cenni, N., Belardinelli, M.E., Marcaccio, M., 2021. The interaction between displacements and water level changes due to natural and anthropogenic effects in the Po Plain (Italy): The different point of view of GNSS and piezometers. J. Hydrol. 596, 126112. http://dx.doi.org/10.1016/j.jhydrol.2021.126112.

Nordstrom, K.F., Armaroli, C., Jackson, N.L., Ciavola, P., 2015. Opportunities and constraints for managed retreat on exposed sandy shores: Examples from Emilia–Romagna, Italy. Ocean Coast. Manag. 104, 11–21. http://dx.doi.org/10.1016/j.ocecoaman.2014.11.010.

Oelsmann, J., Passaro, M., Dettmering, D., Schwatke, C., Sánchez, L., Seitz, F., 2021. The zone of influence: matching sea level variability from coastal altimetry and tide gauges for vertical land motion estimation. Ocean Sci. 17 (1), 35–57. http://dx.doi.org/10.5194/os-17-35-2021.

Palanisamy Vadivel, S.K., Kim, D.-j., Jung, J., Cho, Y.-K., Han, K.-J., 2021. Monitoring the vertical land motion of tide gauges and its impact on relative sea level changes in Korean peninsula using sequential SBAS–InSAR time–series analysis. Remote Sens. 13 (1), http://dx.doi.org/10.3390/rs13010018.

Peltier, W.R., Argus, D.F., Drummond, R., 2015. Space geodesy constrains ice age terminal deglaciation: The global ICE–6G_C (VM5a) model. J. Geophys. Res.: Solid Earth 120, 450–487. http://dx.doi.org/10.1002/2014JB011176.

Perini, L., Calabrese, L., 2010. Il sistema mare–costa dell'Emilia–Romagna. Vol. 20, Pendragon, Bologna, Italy.

Perini, L., Calabrese, L., Luciani, P., Olivieri, M., Galassi, G., Spada, G., 2017. Sea–level rise along the Emilia–Romagna coast (Northern Italy) in 2100: scenarios and impacts. Nat. Hazards Earth Syst. Sci. 17 (12), 2271–2287. http://dx.doi.org/10.5194/nhess-17-2271-2017.

Perissin, D., Ferretti, A., 2007. Urban–target recognition by means of repeated spaceborne SAR images. IEEE Trans. Geosci. Remote Sens. 45 (12), 4043–4058. http://dx.doi.org/10.1109/TGRS.2007.906092.

Pinardi, N., Bonaduce, A., Navarra, A., Dobricic, S., Oddo, P., 2014. The mean sea level equation and its application to the mediterranean sea. J. Clim. 27, 442–447. http://dx.doi.org/10.1175/JCLI-D-13-00139.1.

Pirro, A., Menna, M., Mauri, E., Laxenaire, R., Salon, S., Bosse, A., Martellucci, R., Viboud, S., Valran, T., Hayes, D., Speich, S., Poulain, P.-M., Negretti, M.-E., 2024. Rossby waves driven by the Mid Mediterranean Jet impact the Eastern Mediterranean mesoscale dynamics. Sci. Rep. 14, 29598. http://dx.doi.org/10.1038/s41598-024-80293-6.

Preti, M., Nigris, N.D., Morelli, M., Monti, M., Bonsignore, F., Aguzzi, M., 2008. Emilia–Romagna Littoral State in 2007 and Ten Years Menagement Plan. I quaderni di Arpa.

PSMSL, 2024. Tide gauge data. http://www.psmsl.org/data/obtaining/. (Accessed 19 March 2024).

Romagnoli, C., Bosman, A., Casalbore, D., Anzidei, M., Doumaz, F., Bonaventura, F., Meli, M., Verdirame, C., 2022. Coastal erosion and flooding threaten low-Lying Coastal tracts at lipari (Aeolian Islands, Italy). Remote Sens. 14 (13), 2960. http://dx.doi.org/10.3390/rs14132960.

Sánchez, L., Völksen, C., Sokolov, A., Arenz, H., Seitz, F., 2018. Present–day surface deformation of the Alpine region inferred from geodetic techniques. Earth Syst. Sci. Data 10 (3), 1503–1526. http://dx.doi.org/10.5194/essd-10-1503-2018.

Santamarìa-Gòmez, A., Gravelle, M., Collilieux, X., Guichard, M., Mìguez, B.M., Tiphaneau, P., Wöppelmann, G., 2012. Mitigating the effects of vertical land motion in tide gauge records using a state–of–the–art GPS velocity field. Glob. Planet. Change 98–99, 6–17. http://dx.doi.org/10.1016/j.gloplacha.2012.07.007.

Santer, B.D., Wigley, T.M.L., Boyle, J.S., Gaffen, D.J., Hnilo, J.J., Nychka, D., Parker, D.E., Taylor, K.E., 2000. Statistical significance of trends and trend differences in layer–average atmospheric temperature time series. J. Geophys. Res.: Atmos. 105 (D6), 7337–7356. http://dx.doi.org/10.1029/1999JD901105.

Sen, P.K., 1968. Estimates of the regression coefficient based on Kendall's Tau. J. Amer. Statist. Assoc. 63 (324), 1379–1389. http://dx.doi.org/10.1080/01621459.1968.10480934.

Shirzaei, M., Freymueller, J., Törnqvist, T.E., Galloway, D.L., Dura, T., Minderhoud, P.S.J., 2021. Measuring, modelling and projecting coastal land subsidence. Nat. Rev. Earth Environ. 40–58. http://dx.doi.org/10.1038/s43017-020-00115-x.

Simeoni, U., Tessari, U., Corbau, C., Tosatto, O., Polo, P., Teatini, P., 2017. Impact of land subsidence due to residual gas production on surficial infrastructures: The Dosso degli Angeli field study (Ravenna, Northern Italy). Eng. Geol. 229, 1–12. http://dx.doi.org/10.1016/j.enggeo.2017.09.008.

Soboyejo, L.A., Giambastiani, B.M.S., Molducci, M., Antonellini, M., 2021. Different processes affecting long–term Ravenna coastal drainage basins (Italy): implications for water management. Env. Earth Sci. 80, 493. http://dx.doi.org/10.1007/s12665-021-09774-5.

Sytnik, O., Del Río, L., Greggio, N., Bonetti, J., 2018. Historical shoreline trend analysis and drivers of coastal change along the Ravenna coast, NE Adriatic. Environ. Earth Sci. 77 (23), 779. http://dx.doi.org/10.1007/s12665-018-7963-8.

Sytnik, O., Stecchi, F., 2015. Disappearing coastal dunes: tourism development and future challenges, a case–study from Ravenna, Italy. J. Coast. Conserv. 19, 715–727. http://dx.doi.org/10.1007/s11852-014-0353-9.

Taburet, G., Sanchez-Roman, A., Ballarotta, M., Pujol, M.I., Legeais, J.F., Fournier, F., Faugere, Y., Dibarboure, G., 2019. DUACS DT2018: 25 years of reprocessed sea level altimetry products. Ocean Sci. 15 (5), 1207–1224. http://dx.doi.org/10.5194/os-15-1207-2019.

Taramelli, A., Di Matteo, L., Ciavola, P., Guadagnano, F., Tolomei, C., 2015. Temporal evolution of patterns and processes related to subsidence of the coastal area surrounding the Bevano River mouth (Northern Adriatic) – Italy. Ocean Coast. Manag. 108, 74–88. http://dx.doi.org/10.1016/j.ocecoaman.2014.06.021.

Teatini, P., Ferronato, M., Gambolati, G., Gonella, M., 2006. Groundwater pumping and land subsidence in the Emilia–Romagna coastland, Italy: Modeling the past occurrence and the future trend. Water Resour. Res. 42 (1), http://dx.doi.org/10.1029/2005WR004242.

Teatini, P., Tosi, L., Strozzi, T., 2011. Quantitative evidence that compaction of Holocene sediments drives the present land subsidence of the Po Delta, Italy. J. Geophys. Res.: Solid Earth 116 (B8), http://dx.doi.org/10.1029/2010JB008122.

Tsimplis, M., Calafat, F.M., Marcos, M., Jordà, G., Gomis, D., Fenoglio-Marc, L., Struglia, M.V., Josey, S., Chambers, D.P., 2013. The effect of the NAO on sea level and on mass changes in the Mediterranean Sea. J. Geophys. Res.: Oceans 118, 944–952. http://dx.doi.org/10.1002/jgrc.20078.

Vignudelli, S., Florence, B., Benveniste, J., Fu, L.L., Picot, N., Raynal, M., Roinard, H., 2019. Satellite altimetry measurements of sea level in the coastal zone. Surv. Geophys. 40, 1319–1349. http://dx.doi.org/10.1007/s10712-019-09569-1.

Vilibić, I., Zemunik, P., Dunić, N., Mihanović, H., 2020. Local and remote drivers of the observed thermohaline variability on the northern Adriatic shelf (Mediterranean Sea). Cont. Shelf Res. 199, 104110. http://dx.doi.org/10.1016/j.csr.2020.104110.

Wheeler, H.E., 1964. Baselevel, lithosphere surface, and time–stratigraphy. GSA Bull. 75 (7), 599–610. http://dx.doi.org/10.1130/0016-7606(1964)75[599:BLSAT]2.0.CO;2.

Zerbini, S., Bruni, S., Raicich, F., 2021. Tide gauge data archaeology provides natural subsidence rates along the coasts of the Po Plain and of the Veneto–Friuli Plain, Italy. Geophys. J. Int. 225, 253–260. http://dx.doi.org/10.1093/gji/ggaa602.

Zerbini, S., Raicich, F., Prati, C.M., Bruni, S., Del Conte, S., Errico, M., Santi, E., 2017. Sea–level change in the Northern Mediterranean Sea from long–period tide gauge time series. Earth– Sci. Rev. 167, 72–87. http://dx.doi.org/10.1016/j.earscirev.2017.02.009.